water

MDPI

*Article*

# Impact Response Characteristics of Apron Structure to Bouldery Debris Flow

**Shihua Chen [1], Minghui Meng [2,3,*], Tingting Jiang [1], Jian Guo [4], Dong Sun [2,3], Liang Qin [2,3] and Tiantao Li [1]**

[1] State Key Laboratory of Geohazard Prevention and Geo-Environment Protection, Chengdu University of Technology, Chengdu 610059, China; ch496892763@gmail.com (S.C.)
[2] Sichuan Geological Environment Survey and Research Center, Chengdu 610081, China
[3] Sichuan Engineering Technology Research Center of Geohazard Prevention, Chengdu 610081, China
[4] Department of Civil Engineering, Panzhihua University, Panzhihua 617000, China
* Correspondence: mengmh1990@foxmail.com

**Abstract:** Apron is a commonly used structure in the downstream of debris-flow-retaining dams. Its function is to resist the impact and erosion of debris flow on the dam foundation. In order to enhance the impact resistance of the apron to boulders, increasing the apron thickness and filling the block stone are usually adopted. However, the apron is still often destroyed by bouldery debris flow. Therefore, we propose a kind of toughness apron. Physical test and numerical simulation are used to reveal the dynamic response of the toughness apron. The results show that both tire cushion and stone cushion can buffer the impact of boulders. The physical test showed that the cushion reduces impact force and vibration acceleration, and the numerical simulation results indicate that the cushion significantly reduces damage to the protection apron while dissipating most of the energy. It was also found that there is an energy threshold of impact damage resistance of the apron. When the impact kinetic energy is higher than this threshold, the apron will be damaged. These findings highlight its potential for debris flow protection. According to the corresponding impact characteristics of the dam, the design method of the toughness apron is proposed.

**Keywords:** bouldery debris flow; toughness apron structure; damage analysis; dynamic response; SPH–FEM coupling

check for updates

Academic Editor: Bommanna Krishnappan

Received: 14 January 2025
Revised: 10 February 2025
Accepted: 12 February 2025
Published: 13 February 2025

**Citation:** Chen, S.; Meng, M.; Jiang, T.; Guo, J.; Sun, D.; Qin, L.; Li, T. Impact Response Characteristics of Apron Structure to Bouldery Debris Flow. *Water* **2025**, *17*, 544. https://doi.org/10.3390/w17040544

**Copyright:** © 2025 by the authors. Licensee MDPI, Basel, Switzerland. This article is an open access article distributed under the terms and conditions of the Creative Commons Attribution (CC BY) license (https://creativecommons.org/licenses/by/4.0/).

## 1. Introduction

The Wenchuan earthquake triggered substantial amounts of loose material to slide into gullies, leading to large-scale debris flow disasters in the region, which have occurred frequently over the past decade [1], and resulting in significant loss of life and property damage [2]. In recent years, scholars globally have conducted extensive research on debris flow disaster prevention technologies, proposing numerous measures to effectively mitigate losses caused by debris flows [3]. The retaining dam is a key type of debris flow control structure, commonly employed to intercept solid debris, reduce flow velocity, and stabilize sediment sources within gullies. Retaining dams have been constructed in many debris flow gullies in earthquake-prone regions, though technology for preventing giant debris flows containing boulders remains underdeveloped [4]. After investigating more than 30 debris flow prevention projects, it was found that over-dam erosion is likely when retaining dams are full. Under the impact of boulders and fluid erosion from debris flows, conventional downstream anti-erosion structures, including aprons, auxiliary dams, and submerged dams, gradually fail. In particular, headward erosion from downstream gullies exacerbates

damage to the upstream erosion zone, often resulting in the overhanging of the apron and dam foundation, leading to the instability of the main dam. Statistics indicate that nearly 70% of debris flow prevention projects in Sichuan Province experience apron structure failure due to impact damage, leading to a direct headward erosion of the foundation, which compromises dam stability and leads to project failure. As shown in Figure 1, the aprons were damaged by the impact of boulders.




**Figure 1.** Cases of apron crash damage. (The case occurred in Cutou gully, Wenchuan County, Sichuan Province, China).

Currently, four main anti-impact reinforcement techniques are used for apron structures: the first, filling block stones; the second, increasing the apron's thickness and quality; the third, inserting rails or thick steel plates into the apron; and the fourth, using steel or gabion stone cages. As demonstrated by numerous engineering cases, while these techniques can enhance impact resistance, they do not fully prevent crash damage or headward erosion. Thus, the effective protection of the apron structure is essential for ensuring the continuous and reliable operation of the entire retaining project.

Boulders from debris flows have a destructive impact on rigid structures [5]. Therefore, it is essential to consider boulders in the design of apron structures. In the study of debris flows, it is challenging to fully understanding the dynamic interaction between debris flows and prevention structures through experiments, particularly for bouldery debris flows. Currently, due to the difficulty in accurately measuring the interaction between boulders and debris flow fluid, it is more prudent to calculate the impact force of boulders as an independent load based on their speed in engineering practice. Several semi-empirical methods have been proposed to estimate the maximum impact force of blocks on rigid structures, including Hertz theory, the pulse method, and the energy method [6]. However, the interaction between the debris flow fluid and the blocks depends on factors such as debris flow volume concentration, with the viscous forces in viscous debris flows typically being more significant than those in dilute debris flows [7]. Consequently, numerical methods are now widely employed in debris flow research as they offer clear advantages in revealing features that may be difficult to obtain experimentally [8]. Pan et al. [9] utilized the discrete element simulation software EDEM 2018 to perform numerical simulations of the impact of granular flow on a flume, thereby verifying the reliability of the numerical simulation method. Wang et al. [10] simulated the movement of debris flows using the SPH meshless method, and the results indicated that the SPH method can effectively reproduce the debris flow process. Feng et al. [11] demonstrated that the finite element method can effectively simulate the progressive structural damage caused by debris flow impact. Han et al. [12] utilized their SPH-based numerical model to inverse-calculate the three-dimensional dynamic process of debris flow, thereby obtaining the vertical distribution of

velocity within the cross-section. Luo et al. [13] proposed an SPH–DEM–FEM coupling method for the dynamic study of bouldery debris flow impact on rigid structures; however, the study was limited to the coupling effect of a single boulder with the debris flow slurry and did not address the coupling effects of multiple boulder and their interactions with the debris flow slurry.

Song et al. [14] demonstrated that boulders transported by debris flows are the primary factor causing damage to debris flow protection structures. He et al. [15] investigated the characteristics of the cushion layer subjected to boulders, using a tough rockfall protection structure as the research object, and found that the cushion material plays a beneficial role in reducing the impact force on the protection structure. Chen et al. [16] suggested that an appropriate thickness of the cushion layer is crucial for preventing rockfalls. Sun et al. [17] proposed a rockfall shelter featuring a tire cushion layer and conducted both physical test and numerical simulation, with results indicating that the cushion layer can effectively absorb the impact of rockfalls. Toughness protection net structures are frequently employed to prevent landslides, debris flows, and other geological disasters [18]. Lv [19] proposed a novel spring-lattice debris-flow-retaining structure and analyzed its impact resistance performance, concluding that, compared to a conventional dam, the spring-lattice debris-flow-retaining dam exhibits superior impact resistance. However, there is currently no pertinent research on a toughness protective structure suitable for safeguarding the apron.

In order to enhance the apron's ability to resist boulders in debris flows and extend the service life of the apron structure, this paper proposes a tire–stone composite cushion apron structure for a downstream retaining dam. The tire–stone composite cushion layer is embedded in the concrete of the apron structure, as shown in Figure 2.

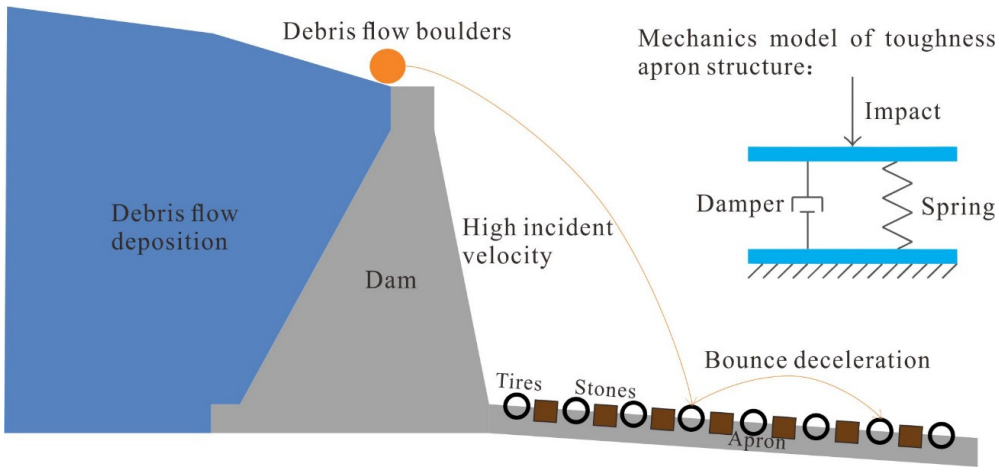



**Figure 2.** Schematic of toughness apron structure.

This paper focuses on the toughness apron structure as the subject of study. First, a rockfall impact test was conducted on various types of toughness aprons to analyze the destruction phenomena and dynamic responses of these structures. Subsequently, a numerical simulation model based on the SPH–FEM coupling algorithm was developed to analyze the structural damage and energy dissipation resulting from the impact of bouldery debris flow on various toughness apron structures. The test results from the rockfall impact test platform and the numerical simulation results were analyzed collectively to verify the scientific effectiveness of the apron structure in mitigating bouldery debris flows. This study offers novel computational insights for the design theory and application of related structures aimed at preventing bouldery debris flows.

## 2. Dynamic Response Analysis of the Toughness Apron Structure Under Rockfall Impact

### *2.1. Test Platform and Physical Simulation Test Design*

The impact test device comprises three components: a rockfall jacking device, a rockfall model, and a data acquisition device, as shown in Figure 3. The rockfall lifting and lowering apparatus is further divided into a rockfall, a steel truss structure, a winch, and an electromagnetic hook release mechanism. The rockfall material is granite, and the rolling and rotation of the stone are disregarded. The rockfall is modeled as a sphere with a radius of 0.1 m and a density of 2500 kg/m$^3$. The height of the truss is 6.00 m, with the top and bottom face dimensions measuring 1.15 m and 2.50 m, respectively. The rockfall can be raised and released using the winch and electromagnetic hook release mechanism, and its fixed height can be controlled to enable the rockfall to freely fall and impact the center of the concrete plate.

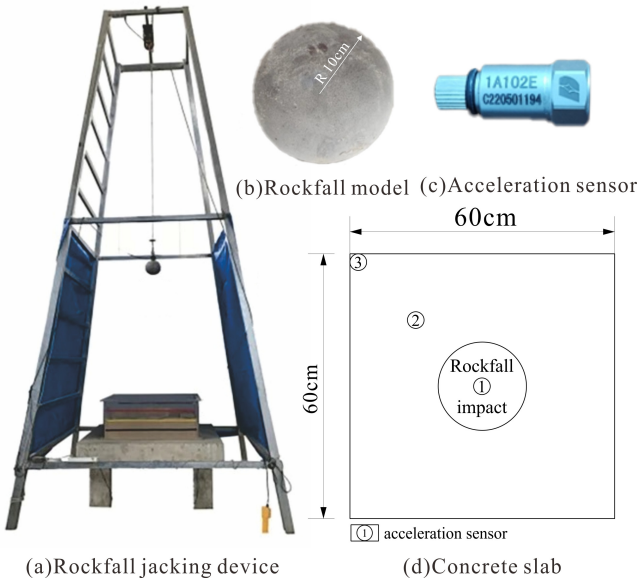



**Figure 3.** Test platform of rockfall impact.

The data acquisition system employs the data acquisition instrument (Jiangsu Donghua Testing Technology Co., Ltd., Taizhou, Jiangsu, China) along with the 1A102E acceleration sensor (Jiangsu Donghua Testing Technology Co., Ltd., Taizhou, Jiangsu, China). The sampling frequency of the acceleration sensor ranges from 1 to 10,000 Hz, with a sensitivity of 1.035 mV/(m·s$^2$) and a maximum range of 500 g. These are installed as shown in Figure 3, with the rockfall positioned on the upper surface, the center of the concrete plate on the lower surface, the diagonal edge of the lower surface, and the center of the diagonal line connecting the lower surface and the inclined side. The direction of the rockfall impact is defined as positive, and the acceleration sensors are connected to the data acquisition instrument, allowing for real-time data collection.

The rockfall impact test is conducted to validate the superior energy-absorbing capabilities of the resilient structure [20] and further investigate the dynamic response characteristics of various toughness structures and concrete slabs. Preliminary tests indicate that when the release height of the rockfall exceeds 2 m, the superior elasticity of the concrete causes the rockfall to rebound significantly after impacting the concrete plate, potentially lifting off from it. To ensure the safe execution of the field test, the rockfall impact height H is established at 2 m. Based on the properties of the toughness structure, this study primarily explores the influence of the energy dissipation effects of concrete with various toughness structures.

The specific experimental scheme was divided into four types: plain concrete slab, tire cushion concrete slab, stone cushion concrete slab, and tire–stone composite cushion concrete slab. For each experimental group, two specimens were prepared to minimize the influence of randomness on the test results. For the plain concrete slab, the mixed concrete was poured directly into the mold and compacted using vibration. For the tire cushion concrete slab and the tire–stone composite cushion concrete slab, half of the tires and stones were embedded, followed by the application of a plastic film to prevent water loss and avoid surface cracking of the concrete pavement specimen. Due to the thinness of the concrete slab, which precluded mechanical vibration compaction, manual compaction was achieved through striking. After casting the test specimens, they were regularly watered for maintenance, and after seven days, they were removed from the mold by tapping the four corners with a rubber hammer to prevent damage to the concrete pavement specimen surface due to insufficient strength. Once the test specimens were removed, they were cleaned, wrapped in plastic, and regularly watered until they were removed from the testing conditions after 28 days. The dimensions of the concrete slab and the casting diagram of the test specimens are illustrated in Figure 4.

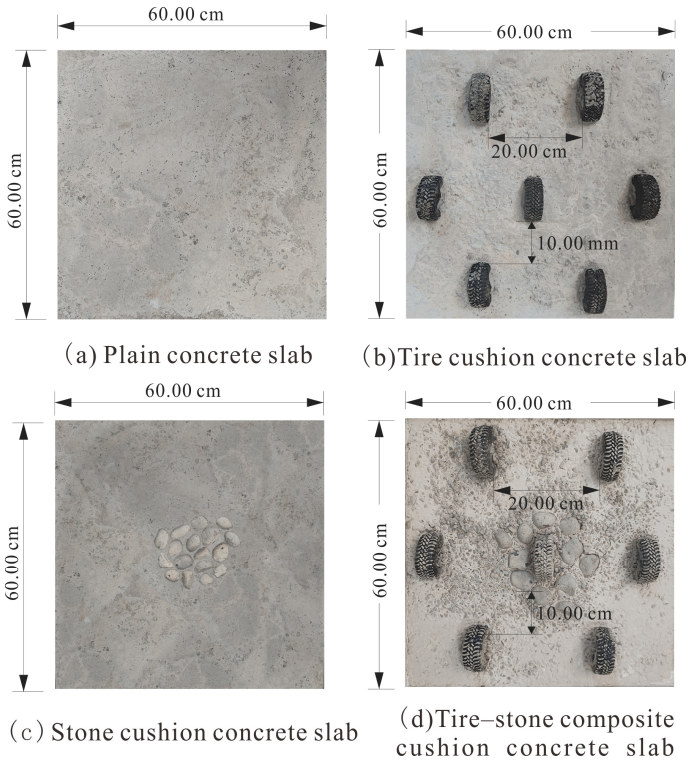



**Figure 4.** Test specimen casting.

### *2.2. Rockfall Impact Test*

As shown in Figure 5, various experimental groups of concrete slabs exhibited different types of damage under rockfall impact. The plain concrete slab sustained damage from the rockfall impact, resulting in a crack pattern resembling an "X". The stone cushion concrete slab also sustained damage, exhibiting a crack pattern resembling a "T". The tire cushion concrete slab sustained damage, with a crack pattern resembling the transverse line. The overall damage pattern exhibited a horizontal crack extending along the central tire, with fewer longitudinal cracks extending from the center to the edge in the stone cushion concrete slab compared to the tire–stone composite cushion concrete slab. The tire–stone composite cushion concrete slab exhibited no obvious signs of damage, while some areas of the stone cushion sustained damage from rockfalls. It is evident that the

damage patterns on the impact surfaces of the plain concrete slab, stone cushion concrete slab, and tire cushion concrete slab are similar, originating from the center point in radial cracks, with only the number of cracks varying. The concrete slab protected by the stone cushion has fewer cracks than the plain concrete slab, while the concrete slab protected by the tire cushion exhibits fewer cracks than the stone cushion concrete slab, and the slab protected by the tire–stone composite cushion shows almost no damage. Based on the observations from the impact test, it can be concluded that the protective effect of the toughness structure on concrete follows the order: tire–stone composite cushion concrete slab > tire cushion concrete slab > stone cushion concrete slab > plain concrete slab.

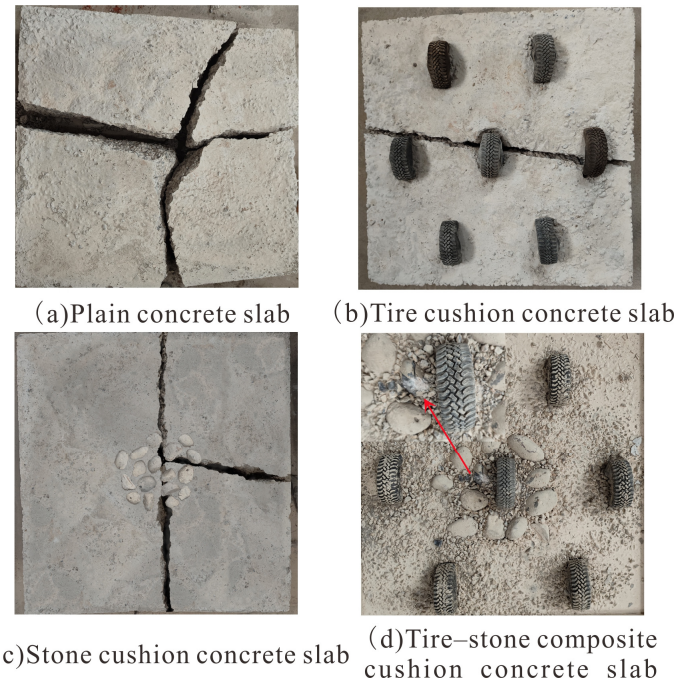



**Figure 5.** Test failure phenomenon.

### *2.3. Dynamic Response Analysis of Different Concrete Slab Under Impact*

As shown in the curve of rockfall impact force with time in Figure 6, the impact force quickly reaches its peak value when the rockfall contacts the surface of the concrete slab. Upon the transmission of the impact force to the concrete slab, the force rapidly decreases. Furthermore, the analysis of the figure indicates that the peak impact forces of the stone cushion concrete slab, tire cushion concrete slab, and tire–stone composite cushion concrete slab are all smaller than plain concrete slab. Specifically, the peak impact force of the plain concrete slab decreases from 31.56 kN to 25.72 kN, representing a reduction of approximately 18.50%. In comparison, the tire cushion concrete slab exhibited a decrease from 31.56 kN to 12.49 kN, a reduction of approximately 60.42%. Similarly, the tire–stone composite cushion concrete slab showed a decrease from 31.56 kN to 20.15 kN, representing a reduction of approximately 36.15%. The duration of the initial impact starts with the rockfall contacts the slab and ends with the rockfall rebounds off the concrete slab. According to the figure, under the impact of rockfall at the same height and weight, the impact durations of the tire cushion concrete slab and the tire–stone composite cushion concrete slab are notably longer than the plain concrete slab. The rockfall impact forces of the plain concrete slab and stone cushion concrete slab are not hindered by impact, allowing the kinetic energy of the rockfall to be directly transferred to the concrete slab. In contrast, the kinetic energy of the rockfall decreases gradually when it hits the cushioned slabs. The tire cushion and tire–stone composite cushion slow down the impact due to the tire and

stone acting as obstacles to the rockfall's motion. Subsequently, the tire cushion concrete slab impacts the concrete slab and remains on it, absorbing a portion of the rockfall's kinetic energy through the tire buffer. In contrast, the concrete slab with the tire–stone composite cushion impacts the stone cushion after the tire compresses, absorbing part of the kinetic energy, resulting in a rapid decrease in impact force. However, in comparison to the tire cushion, the stone cushion enhances the overall stiffness of the cushion.

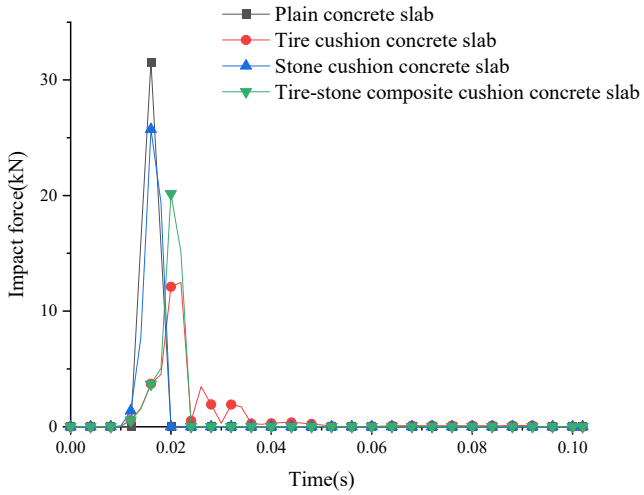



**Figure 6.** Variation of rockfall impact force with time.

When the rockfall impacted the concrete slab, the resulting stress causes the slab bottom to vibrate. As shown in Figure 7, the peak acceleration of the vibration at the center of the plain concrete slab bottom is 11.23 g. As the distance from the center of the top slab increases, the acceleration values gradually decrease, reflecting the trend of the stress wave generated by the rockfall's impact on the concrete slab, which spread out and gradually dissipates at the slab bottom. Significant acceleration occurs on the slab bottom due to tires' high rebound characteristics and generates a peak vibration acceleration of 6.37 g. The tires on the stone cushion generate lower vibration acceleration than the plain concrete slab but higher than the tire cushion concrete slab, with a peak acceleration of 7.71 g due to the stiffness of the surface stones. The tire–stone composite cushion concrete slab exhibits the smallest vibration acceleration at all measurement points, with a peak acceleration of 3.39 g.

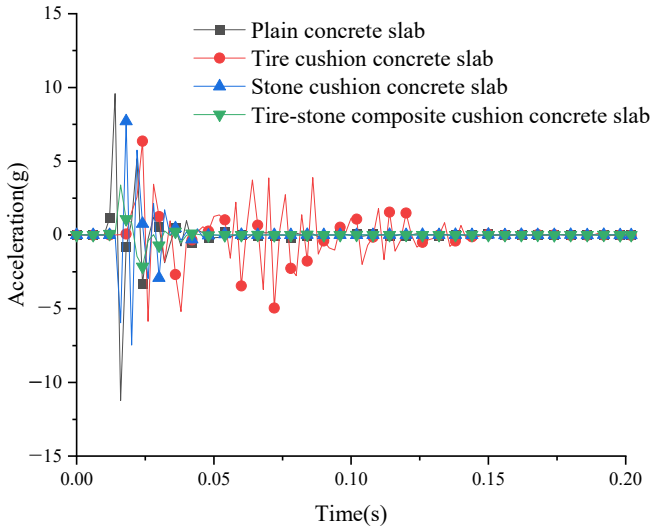



**Figure 7.** Variation of plate bottom acceleration with time.

As shown in Figure 8, the peak acceleration of vibration at the center of concrete slab bottom under rockfall impact is as follows: plain concrete slab > stone cushion concrete slab > tire cushion concrete slab > tire–stone composite cushion concrete slab. The reduction in peak acceleration at the concrete slab bottom effectively evaluated that the tire cushion, stone cushion, and tire–stone composite cushion all exhibit good shock absorption effects. By comparing vibration accelerations at different positions of the slab bottom, the best shock absorption is revealed. The tire–stone composite cushion performs the best in reducing the impact of rockfalls on the concrete slab.

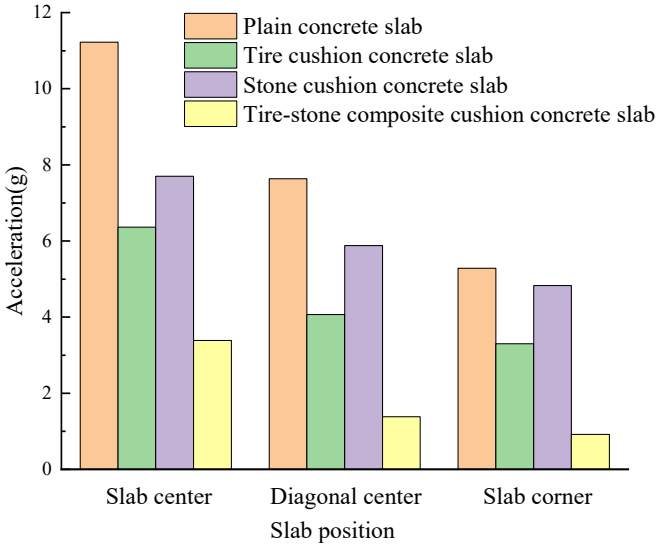



**Figure 8.** Vibration peak acceleration at different positions of the plate bottom.

## 3. Toughness Apron Structure Damage and Energy Analysis

### *3.1. Computational Model Simplification*

#### 3.1.1. Geometric Model

Figure 9 shows the geometric model, consisting of a retaining dam, debris flow deposition, debris flow slurry, boulders, apron, tires, and filler stones. This study aims to qualitatively examine the mechanical behavior of the apron structure under the impact of debris flow containing boulders at full reservoir conditions. To simplify the model, the flexibility of the sediment deposit is temporarily ignored, assuming that both the bottom and sides of the sediment deposit are planar. The dam heights are 10 m, 20 m, and 30 m, with a length of 30 m. The concrete apron structure connects to the bottom of the dam, with a length of 50 m and a width of 30 m. The sediment deposit is considered to be in a full reservoir condition, with its shape and size established based on the dimensions of the corresponding dam. The top length of the sediment deposit is 25 m, with a width of 30 m and a height determined by the various dam heights. There are four types of boulders, with dimensions of 0.5 m, 1 m, 2 m, and 3 m, with five boulders of each type. The debris flow slurry is positioned along the centerline of the dam and sediment deposit, measuring 15 m in length, 10 m in width, and 6 m in height. The outer diameter of the tire is 1 m, the inner diameter is 0.5 m, and the thickness is 0.3 m. During the modeling process, to manage complexity and reduce computational volume, the tire is modeled as being half embedded in the concrete apron structure, considering only its half. The tire–stone composite cushion concrete is modeled similarly to the tire model, focusing solely on the surface of the concrete apron structure, with block stone dimensions of 2 m × 2 m × 0.4 m.

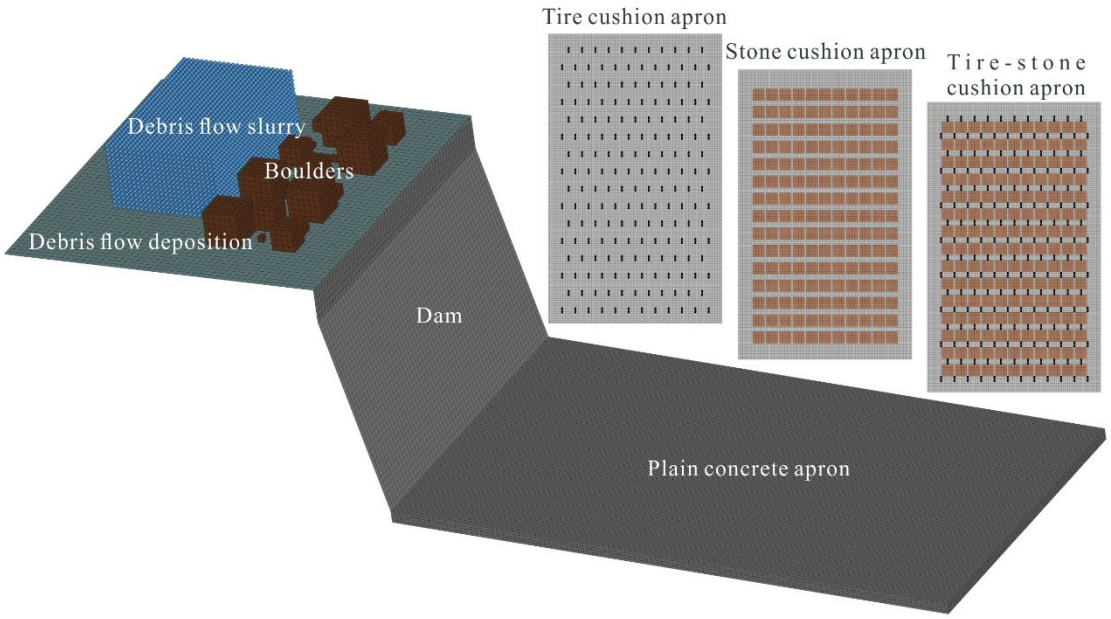



**Figure 9.** Schematic of calculation model.

#### 3.1.2. Material Models

In order to simulate the deformation of the new debris flow apron subjected to impacts from boulders, the LS-DYNA (Version R13.00) material library's rigid material model (*MAT_RIGID) is used for the deposition body and retaining dam simulations to improve computational efficiency and prevent penetration phenomena. The boulders are mostly granite, which have small deformation and high strength. Therefore, they can be considered rigid during impact. Consequently, they are also simulated using the rigid material model (*MAT_RIGID), with material parameters listed in Table 1.

**Table 1.** Rigid body material parameters.

| $\rho_0$/kg/m$^3$ | *E*/Pa | $\nu$ |
|---|---|---|
| 2500 | $3 \times 10^{10}$ | 0.24 |

The apron is cast with C30 plain concrete, and various concrete constitutive models are available in LS-DYNA. In this study, the concrete material is designed using the HJC model (*MAT_JOHNSON_HOLMQUIST_CONCRETE), which allows for parameter adjustments to quantify concrete failure due to debris flow impact. According to the failure criterion set by Liu Chun et al. [21], the simulation utilizes the maximum principal strain failure criterion. When the maximum principal strain exceeds 0.05, the concrete element fails. The material parameters are listed in Table 2.

**Table 2.** Concrete material parameter.

| $\rho_0$/kg/m$^3$ | *G*/Pa | *A* | *B* | *C* | *N* | $F_c$/Pa |
|---|---|---|---|---|---|---|
| 2440 | $1.486 \times 10^{10}$ | 0.79 | 1.6 | 0.007 | 0.61 | $34.2 \times 10^6$ |
| $T$/Pa | $\varepsilon_0$/s$^{-1}$ | $\varepsilon_{fmin}$ | $S_{\max}$ | $P_{crush}$/Pa | $\mu_{crush}$ | $P_{lock}$/Pa |
| $3.63 \times 10^6$ | 1 | 0.01 | 7.0 | $11.4 \times 10^6$ | 0.001 | $8.0 \times 10^8$ |
| $\mu_{lock}$ | $D_1$ | $D_2$ | $K_1$/Pa | $K_2$/Pa | $K_3$/Pa | — |
| 0.1 | 0.04 | 1.0 | $8.5 \times 10^{10}$ | $17.1 \times 10^{10}$ | $20.8 \times 10^{10}$ | — |

The tire is modeled using a segmented elastoplastic material model (*MAT_PIECE-WISE_LINEAR_PLASTICITY), which defines the strain rate effect based on the stress–strain curve. This model is particularly suited for tire modeling, and its material parameters are listed in Table 3.

**Table 3.** Tire material parameter.

| $\rho_0$/kg/m$^3$ | $\sigma_s$/Pa | *PR* | *G*/Pa | *C* | *P* |
|---|---|---|---|---|---|
| 1000 | $2.0 \times 10^{11}$ | 0.3 | $2.0 \times 10^{8}$ | 40 | 5 |

The debris flow slurry exhibits properties of a non-Newtonian fluid, resulting in complex dynamic characteristics. The slurry constitutive relationship is modeled using the non-Newtonian Herschel–Bulkley material model, with a density of 1600 kg/m$^3$ and a yield stress of 2.9 Pa, as determined by the Fei [22] equation based on the fitting results of Yang et al. [23] for various debris flow slurry rheological parameters. A stiffness coefficient is calculated using linear interpolation of Li's [24] experimental results, and a state equation is defined using the weakly compressible Gruneisen state equation. The material parameters are listed in Table 4.

**Table 4.** Model parameters of debris flow slurry.

| $\rho_0$/kg/m$^3$ | $\tau_0$/Pa | *k*/pa·s | *n* | C/m/s | $S_1$ | $\gamma_0$ |
|---|---|---|---|---|---|---|
| 1600 | 2.9 | 1.66 | 0.4 | 1480 | 1.79 | 1.65 |

#### 3.1.3. Calculation Units

The deposition body and the retaining dam are simulated utilizing the shell163 element to enhance computational efficiency. The boulders, apron, tires, and filler stones between the tires are modeled using the solid164 three-dimensional solid element with eight nodes. These elements support nonlinear analyses, are suitable for large deformation simulations, and operate under sandbox control. The mudstone slurry is simulated using the SPH particle method.

#### 3.1.4. Boundary Conditions

Simplified boundary conditions are applied to the model reflecting actual conditions. The bottom of the retaining dam is subjected to fixed constraints to improve computational efficiency. Since the dam shoulder is embedded in the mountain on both sides, fixed constraints are applied to both sides of the retaining dam shoulder. The bottom of the river is similarly constrained. Additionally, a rigid wall (*RIGIDWALL_PLANAR) is placed on both sides as the boundary constraint for boulders and debris flow slurry.

This paper considers the extreme flow velocities of debris flows, setting the initial velocities of boulders and debris flow slurry exiting the dam body to 5 m/s and 10 m/s, respectively, and applying a gravitational acceleration of 9.81 m/s$^2$. The friction coefficients between the debris flow slurry and the deposit, retaining dam, apron, and tire are set to 0.12, while the friction coefficients between the boulders and the deposit, retaining dam, apron, tire, tire-filling stones, and debris flow slurry are set to 0.4.

In order to reproduce the entire process of debris flow impacting the apron, the calculation time is set to 12 s.

### *3.2. Numerical Working Condition Design*

A total of 12 working conditions were designed for the numerical simulation in this study, all utilizing simplified calculation models (Table 5). The first six conditions

controlled the height of the dam body and the speed of the debris flow to investigate the energy damage inflicted on the toughness apron structure by varying heights and speeds. The last six conditions controlled the speed of the dam body and the type of apron to investigate the energy damage experienced by different types of aprons under fixed height and variable speed impacts. The height of the dam body was divided into 10 m, 20 m, and 30 m; the speed of debris flow was divided into 5 m/s and 10 m/s; and the type of apron included plain concrete apron, tire cushion apron, stone cushion apron, and tire–stone composite cushion apron.

**Table 5.** Calculated operating condition in simulation. (The PCA represents the plain concrete apron, the TCA represents the Tire cushion apron, the SCA represents the Stone cushion apron, and the TSCA represents the tire–stone composite cushion apron).

| **Working Condition** | **1** | **2** | **3** | **4** | **5** | **6** | **7** | **8** | **9** | **10** | **11** | **12** |
|---|---|---|---|---|---|---|---|---|---|---|---|---|
| Apron type | PCA | PCA | PCA | PCA | PCA | PCA | TCA | TCA | SCA | SCA | TSCA | TSCA |
| Dam height (m) | 10 | 10 | 20 | 20 | 30 | 30 | 20 | 20 | 20 | 20 | 20 | 20 |
| Debris flow velocity (m/s) | 5 | 10 | 5 | 10 | 5 | 10 | 5 | 10 | 5 | 10 | 5 | 10 |

### *3.3. Analysis of Numerical Simulation Results*

#### 3.3.1. Impact Damage Analysis

In general, the larger the stress value, the more likely the material is to crack [25]. Figure 10 shows the maximum Von Mises stress of the apron under different impact heights, speeds, and apron types. It can be observed that as the impact height and speed increase, the maximum Von Mises stress of the apron rises, occurring at the 3 m sized block impact location. Additionally, as the impact speed increases, the maximum Von Mises stress hierarchy follows: plain concrete apron > stone cushion apron > tire cushion apron > tire–stone composite cushion apron.

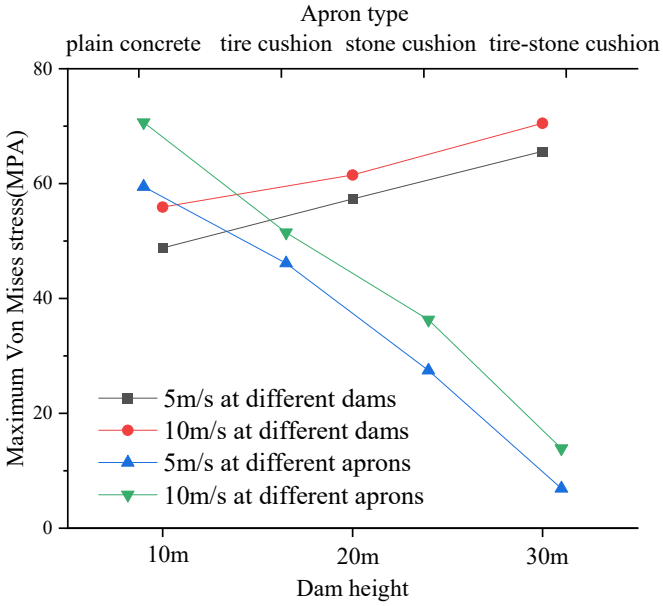



**Figure 10.** Maximum Von Mises stress under different working conditions.

By setting the failure criterion of concrete elements in the K file, the damage to concrete under impact can be more accurately reproduced. In this study, a maximum principal strain of 0.05 is adopted as the failure criterion. Figure 11 shows the statistical number of failed concrete elements under different impact heights and speeds, as well as varying types of toughness aprons. It can be observed from the figure that as the impact height and speed

increase, the number of failed concrete elements correspondingly increases. Furthermore, as the impact speed increases, the hierarchy of failed concrete elements is as follows: plain concrete apron > stone apron > tire apron > stone–tire composite apron. The stone–tire composite apron structure exhibits minimal damage.

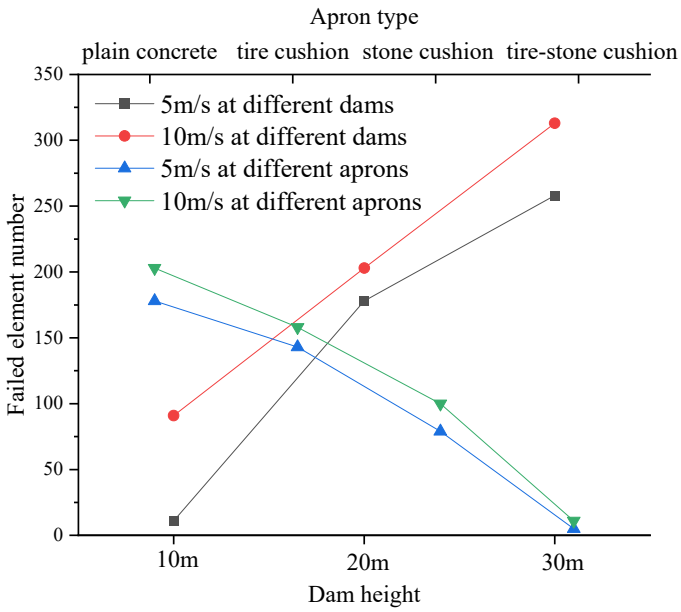



**Figure 11.** Failure element under different working conditions.

### 3.3.2. Impact Energy Analysis

In Section 3.3.1, the damage to the toughness apron structure is compared under different conditions. In this section, we analyze the energy of the stones to obtain the failure and destruction energy threshold of the concrete in the apron. Due to the interaction between the debris flow slurry and boulders, the kinetic energy of similarly sized stones exhibits differences. In the first working condition, at t = 2~4 s, the kinetic energy of the 3 m sized stones reaches its peak value. The minimum kinetic energy required for the toe protection concrete to fail is 8522 kJ, while the maximum kinetic energy that does not cause failure is 5174 kJ. In the second working condition, at t = 1~3 s, the kinetic energy of the 3 m sized stones also reaches its peak value. The minimum kinetic energy required for the apron to fail is 8390 kJ, while the maximum kinetic energy that does not cause failure is 7710 kJ. In the third working condition, at t = 2~4 s, the kinetic energy of the 2 m sized stones reaches its peak value. The minimum kinetic energy required for the apron to fail is 5295 kJ, while the maximum kinetic energy that does not cause failure is 4029 kJ. In the fourth working condition, at t = 2~4 s, the kinetic energy of the 2 m sized block stones also reaches its peak value. The minimum kinetic energy causing failure to the apron is 5592 kJ, while the maximum kinetic energy that does not cause failure is 5032 kJ. In the fifth working condition, at t = 3~4 s, the kinetic energy of the 2 m sized block stones reaches its peak value, with the minimum kinetic energy causing failure to the apron at 6437 kJ. In the sixth working condition, at t = 2~4 s, the kinetic energy of the 2 m sized stones also reaches its peak value, with the minimum kinetic energy causing failure to the apron at 6414 kJ. Based on the minimum kinetic energy causing failure to the apron and the maximum kinetic energy not causing failure across the aforementioned working conditions, it can be concluded that the energy threshold for the stones to induce failure and damage to the apron ranges from 5174 kJ to 5295 kJ. Notably, the maximum kinetic energy of the stones that does not cause failure in the second working condition is 7710 kJ, which presents a conflict with the established energy threshold for the apron to sustain failure and damage.

The analysis of the numerical simulation of the debris flow movement process in the second working condition reveals that the boulders with a maximum kinetic energy of 7710 kJ did not impact the apron at the moment of peak kinetic energy. Instead, they first impacted other boulders, transferring part of their kinetic energy, and subsequently impacted the apron with kinetic energy below the failure threshold, resulting in their inability to cause failure and damage to the apron, as shown in Figure 12.

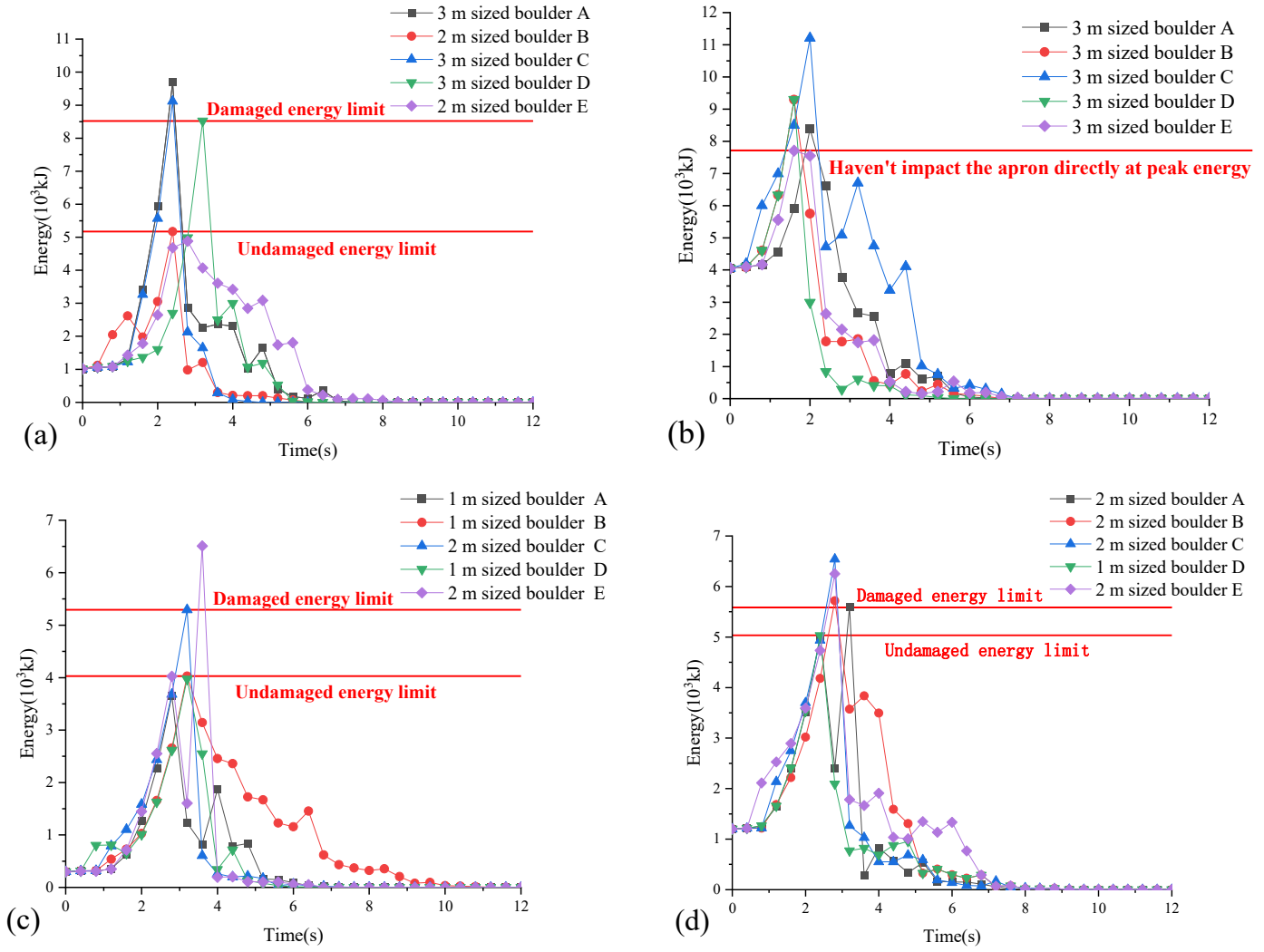



**Figure 12.** Failure energy threshold of plain concrete apron. ((**a**) Working conditions 1; (**b**) working conditions 2; (**c**) working conditions 3; (**d**) working conditions 4).

To investigate the impact resistance performance of various types of toughness apron structures, we extracted the curves of internal energy with time for different types of toughness apron structures at debris flow velocities of 5 m/s and 10 m/s, each under an impact height of 20 m. As shown in Figure 13, the initial internal energy of the apron is 0. At approximately t = 2 s, the debris flow boulders begin to impact the toughness aprons structures. Some of the kinetic energy from the boulders is transferred to the apron via the stone cushion as rigid damping, converting into the internal energy of the apron. Some is converted into elastic potential energy and the internal energy of the tires after impacting them through elastic damping. Some is rebounded by the apron, converting into the gravitational potential energy of the boulders. Some is consumed and converted into heat energy through friction with the apron. Subsequently, it falls again for energy conversion and ultimately either remains on or leaves the apron. At t = 8 s, the internal energy of the

apron reaches its peak value and stabilizes. By comparing the internal energy of various toughness apron structures at the same impact height and velocity, we observe that the internal energy follows the order: plain concrete apron > stone cushion apron > tire cushion apron > tire–stone composite cushion apron, with the internal energy of the tire–stone composite cushion apron being significantly smaller than the other aprons.

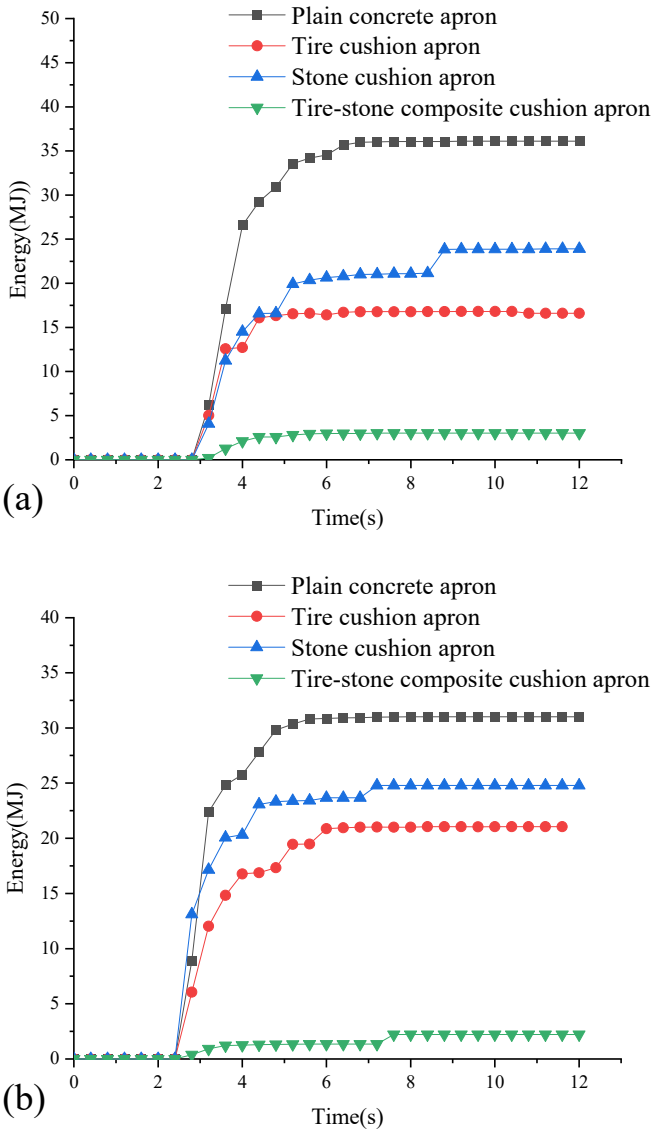



**Figure 13.** Variation of apron internal energy with time. ((**a**) The speed of 5 m/s at a dam height of 20 m corresponds to working conditions 3, 7, 9, and 11; (**b**) the speed of 10 m/s at a dam height of 20 m corresponds to working conditions 4, 8, 10, and 12).

Notably, according to the energy curve with time of the apron in Figure 13, at the same height, the kinetic energy of debris flows with higher initial velocities is expected to be greater; however, aprons made of plain concrete absorb less internal energy due to differences in the debris flow impact angle. Figure 14 presents the sliding energy curve with the time of the plain concrete apron at height of 20 m, impacted by debris flows with velocities of 5 m/s and 10 m/s. The debris flow with a higher initial velocity impacts the apron at a smaller angle, resulting in horizontal frictional sliding energy from the 10 m/s debris flow being approximately twice that of the 5 m/s debris flow.

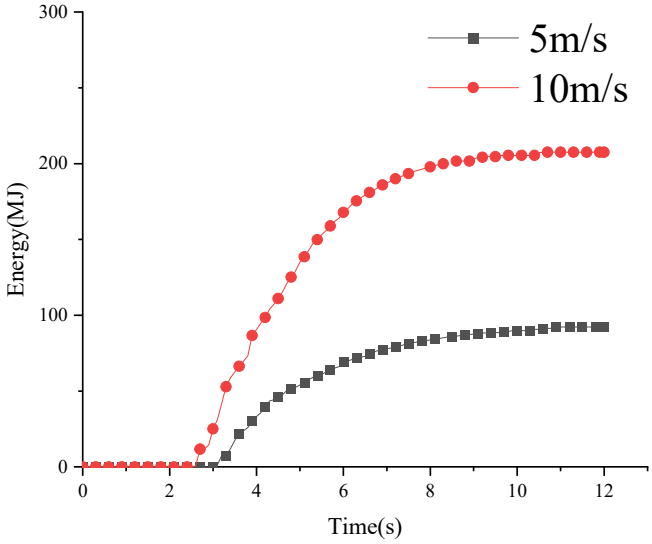



**Figure 14.** Variation of apron slide energy with time.

## 4. Discussion

Based on the above results, a comparison (Table 6) of the experimental and numerical results has been included. The results show good consistency, with the buffering performance ranking in the following order: plain concrete apron < stone cushion apron < tire cushion apron < tire–stone composite cushion apron.

**Table 6.** Comparison of experimental and numerical results.

| Apron Type | Experimental Results | Numerical Results |
|---|---|---|
| Plain concrete apron | \ | \ |
| Tire cushion apron | Impact forces and vibration acceleration reduced slightly | Von Mises stress and internal energy reduced slightly |
| Stone cushion apron | Impact forces and vibration acceleration reduced significantly | Von Mises stress and internal energy reduced significantly |
| Tire–stone composite cushion apron | Impact forces and vibration acceleration reduced maximally | Von Mises stress and internal energy reduced maximally |

Due to the limitations of experimental conditions, conducting direct physical simulation experiments on the over-dam impact of bouldery debris flows to the apron under full reservoir conditions is not feasible. Therefore, a numerical simulation method based on SPH–FEM coupling is employed. However, the complexity of the model prevents an accurate extraction of interaction forces between individual boulders and the structures, allowing only macroscopic analysis in terms of stress, damage, and energy. Simultaneously, a rockfall impact test is conducted to study the dynamic response of a toughness structure concrete slab to a single boulder. As mentioned in Section 3.3.2, debris flow impacts occur at an angle, whereas the rockfall impact test involves vertical impacts, which do not capture the effects of horizontal velocity components. The test can be optimized by tilting the concrete slab at different angles for rockfall impacts, allowing the verification of the differences in dynamic response caused by impact angles.

In the energy analysis of the numerical simulation, it was found that, across various conditions, the minimum kinetic energy of boulders that caused failure and damage to the apron can be approximated by the maximum kinetic energy of boulders that did not cause failure. When the impact kinetic energy of the boulders exceeds this threshold, they can cause damage to the concrete. According to the kinetic energy theorem, the peak kinetic

energy $E_k$ of boulders getting over the dam and striking the apron before impact is the sum of their initial kinetic energy and gravitational potential energy, where m is the mass of the boulder, $V_0$ is the initial velocity of the boulder over the dam, $g$ is the gravitational acceleration 9.80 m/s$^2$, and $h$ is the dam height:

$$E_k = \frac{mv_0^2}{2} + mgh \tag{1}$$

The kinetic energy of the boulder impacting the apron must be less than or equal to the approximate threshold of apron energy destruction $E_0$:

$$m(\frac{v_0^2}{2} + gh) \leq E_0 \tag{2}$$

Assuming the boulder is a regular cuboid with edge length $a$,

$$\rho a^3(\frac{v_0^2}{2} + gh) \leq E_0 \tag{3}$$

In this simulation, the density of the boulder $\rho$ is set at 2500 kg/m$^3$, and gravitational acceleration $g$ is taken as 9.81 m/s$^2$. The approximate threshold value of toe energy destruction $E_0$, obtained from this simulation, is 5000 kJ. The size of the boulder to be prevented at various dam heights and debris flow velocities can be calculated using this formula:

$$a \leq \sqrt[3]{\frac{4000}{(v_0^2 + 19.62h)}} \tag{4}$$

The boulder sizes that should be prevented for 10 m, 20 m, and 30 m dams at debris flow velocities of 5 m/s and 10 m/s can be determined using Formula (4), aiding in the optimization of engineering applications by strategically arranging the toughness structure. However, this study mainly focuses on the toughness cushion structure, and the apron model was simplified by adjusting the material parameters and failure criteria. The damage energy threshold obtained can provide valuable insights for future downstream erosion protection projects (Table 7).

**Table 7.** Size of block rock to prevent at different dam heights and debris flow velocities.

| Height (m) \ Velocity (m/s) | 5 | 10 |
|---|---|---|
| 10 | 3 m sized boulder | 3 m sized boulder |
| 20 | 2 m sized boulder | 2 m sized boulder |
| 30 | 2 m sized boulder | 2 m sized boulder |

## 5. Conclusions

This study investigates the impact response of apron structures under bouldery debris flow conditions through rockfall impact tests and numerical simulations. The damage characteristics, energy dissipation, and dynamic response were analyzed to evaluate the effectiveness of a toughness apron structure for mitigating bouldery debris flow impact. The key conclusions are as follows:

(1) Both tire and stone cushions effectively reduce the impact of boulders in debris flow, significantly decreasing rockfall impact forces and the vibration acceleration of the concrete slab.

(2) Filling the tire cushion with stone cushion substantially enhances the apron's toughness and energy dissipation capacity, improving its ability to withstand boulder impacts.
(3) The impact resistance of the apron can be characterized by an energy threshold. When the impact kinetic energy is higher than this threshold, it will cause damage to the apron.

The apron's impact resistance can be characterized by an energy threshold. When the impact kinetic energy exceeds this threshold, structural damage occurs, indicating a critical design parameter for apron resistance.

**Author Contributions:** Investigation, M.M., D.S. and L.Q.; Methodology, J.G.; Software, T.J.; Supervision, T.L.; Writing—Original Draft, S.C.; Writing—Review and Editing, T.L. and S.C.; Funding Acquisition, T.L. All authors have read and agreed to the published version of the manuscript.

**Funding:** This research was funded by the National Natural Science Foundation of China (42377194), the Sichuan Province Central Government Guides Local Science and Technology Development Special Project (2023ZYD0151), and the State Key Laboratory of Geohazard Prevention and Geo-environment Protection Independent Research Project (SKLGP2021Z008). The APC was funded by the Sichuan Province Central Government Guides Local Science and Technology Development Special Project (2023ZYD0151).

**Data Availability Statement:** Some or all of the data, models, or code that support the findings of this study are available from the corresponding author upon reasonable request.

**Acknowledgments:** The authors would like to express their sincere gratitude to all the fundings for their financial support of this project.

**Conflicts of Interest:** Authors Minghui Meng, Dong Sun, and Liang Qin were employed by the company Sichuan Geological Environment Survey and Research Center. The remaining authors declare that the research was conducted in the absence of any commercial or financial relationships that could be construed as a potential conflict of interest.

## References

1. Huang, H.; Zhao, Q. Basic characterustucs and preliminary mechanism analysis of large scale rockslide-sturzswtrom at Wenjiagou triggered by Wenchuan earthquake. *J. Eng. Geol.* **2010**, *18*, 168. (In Chinese)
2. Cui, P.; Zhuang, J.; Chen, X.; Zhang, J.; Zhou, X. Characteristics and Countermeasures of Debris Flow in Wenchuan Area After the Earthquake. *J. Sichuan Univ. Eng. Sci. Ed.* **2010**, *42*, 10–19. (In Chinese)
3. Wang, J.; Jin, C.; Yuan, H.; Wang, X.; Fang, W.; Sun, J.; Wang, Z. Numerical simulation and countermeasures of potential debris flow disasters in Yanqing competition area of Olympic Winter Games Beijing 2022. *J. Eng. Geol.* **2023**, *31*, 514–525. (In Chinese)
4. Song, G.; Zhang, J.; Yang, Z. Effectiveness Evaluation and Problems Analysis of Debris Flow Control Project after Earthquake. *J. Catastrophology* **2022**, *37*, 58–67. (In Chinese)
5. Shen, W.; Zhao, T.; Dai, F.; Crosta, G.B.; Wei, H. Discrete Element Analyses of a Realistic-shaped Rock Block Impacting Against a Soil Buffering Layer. *Rock Mech. Rock Eng.* **2020**, *53*, 3807–3822. [CrossRef]
6. He, S.M.; Wu, Y.; Shen, J.; Institute of Mountain Hazards and Environment. Simplified calculation of impact force of massive stone in debris flow. *J. Nat. Disasters* **2009**, *18*, 51–56. (In Chinese)
7. Ng, C.W.W.; Liu, H.; Choi, C.E.; Kwan, J.S.H.; Pun, W.K. Impact dynamics of boulder-enriched debris flow on a rigid barrier. *J. Geotech. Geoenviron. Eng.* **2021**, *147*, 04021004. [CrossRef]
8. Zhao, L.; He, J.W.; Yu, Z.X.; Liu, Y.P.; Zhou, Z.H.; Chan, S.L. Coupled numerical simulation of a flexible barrier impacted by debris flow with boulders in front. *Landslides* **2020**, *17*, 2723–2736. [CrossRef]
9. Pan, Q.; Zhang, Q.; Li, Y. Discrete element simulation study of debris flow movement law and impact performance. *J. Eng. Geol.* **2020**, *28*, 1057–1065. (In Chinese)
10. Wang, S.R.; Li, C.Y.; Zou, Z.S.; Liu, X.L. Acoustic emission characteristics of instability process of a rock plate under concentrated loading. *Fract. Struct. Integr* **2016**, *10*, 182–190. [CrossRef]
11. Feng, S.J.; Gao, H.Y.; Gao, L.; Zhang, L.M.; Chen, H.X. Numerical modeling of interactions between a flow slide and buildings considering the destruction process. *Landslides* **2019**, *16*, 1903–1919. [CrossRef]

12. Han, Z.; Zeng, C.; Li, Y.; Chen, G.; Chen, N.; Hu, G.; Xu, L. Nonlinear vertical velocity distribution of debris flows using fluid-particle hierarchical statistical algorithm. *J. Eng. Geol.* **2023**, *31*, 893–904. (In Chinese)
13. Luo, G.; Zhao, Y.J.; Shen, W.G.; Wu, M. Dynamics of bouldery debris flow impacting onto rigid barrier by a coupled SPH-DEM-FEM method. *Comput. Geotech.* **2022**, *150*, 104936. [CrossRef]
14. Song, D.; Choi, C.E.; Zhou, G.G.D.; Kwan, J.S.; Sze, H.Y. Impulse load characteristics of bouldery debris flow impact. *Géotechnique Lett.* **2018**, *8*, 111–117. [CrossRef]
15. He, S. Calculation of Compact Pressure of Rock-fall on Shield Structures. *Eng. Mech.* **2010**, *27*, 175–180. (In Chinese)
16. Chen, T.; Xiang, X.; Zhang, G. Hertz theory based study on punching characteristics of rockfall impacting on shed-tunnel structure. *J. Eng. Geol.* **2023**, *31*, 199–206. (In Chinese)
17. Sun, J.H.; Chu, Z.J.; Liu, Y.F.; Luo, W.; Wang, M. Performance of used tire cushion layer under rockfall impact. *Shock Vib.* **2016**, *2016*, 8760592. [CrossRef]
18. Liu, C.; Chen, L.; Chen, C.; Wei, T. Experimental study on the passive flexible protection under the rock-fall impact. *Chin. J. Geol. Hazard Control* **2014**, *25*, 37–44. (In Chinese)
19. Lv, Z. Study on Impact Resistance of Spring Lattice Debris Flow Dam. Master's Thesis, Lanzhou University of Technology, Lanzhou, China, 2014. (In Chinese).
20. Wang, D.; Yi, X.; Zhou, L.; Yan, S.; Liu, Y. Dynamic response of open cut tunnel with EPE-sand composite cushion under rolling stone impact. *J. Vib. Shock* **2022**, *41*, 201–210. (In Chinese)
21. Liu, C.; Yu, Z.; Luo, L.; Gu, S.; Zhao, S. Dynamic behavior of a concrete dam impacted by debris flows with rock. *J. Vib. Shock* **2019**, *38*, 161–168, 238. (In Chinese)
22. Fei, X. A Model for calculating viscosity of sediment carrying flow in the middle and lower Yellow River. *J. Sediment Res.* **1991**, *2*, 1–13. (In Chinese)
23. Yang, H.; Hu, K.; Wei, F. Methods for computing rheological parameters of debris-flow slurry and their extensibilities. *J. Hydraul. Eng.* **2013**, *44*, 1338–1346. (In Chinese)
24. Li, P.; Liang, D. Volume weight of debris flow and its calculation. *J. Sediment Res.* **1982**, *3*, 75–83. (In Chinese)
25. Guan, W.; Du, Q.; Liu, P. Finite element analysis of the sealing performance of rubber O-ring. *Lubr. Eng.* **2012**, *37*, 60–64. (In Chinese)

**Disclaimer/Publisher's Note:** The statements, opinions and data contained in all publications are solely those of the individual author(s) and contributor(s) and not of MDPI and/or the editor(s). MDPI and/or the editor(s) disclaim responsibility for any injury to people or property resulting from any ideas, methods, instructions or products referred to in the content.